AJNR

Mesoscopic Assessment of Microstructure in Glioblastomas and Metastases by Merging Advanced Diffusion Imaging with Immunohistopathology

Urs Würtemberger, Daniel Erny, Alexander Rau, Jonas A. Hosp, Veysel Akgün, Marco Reisert, Valerij G. Kiselev, Jürgen Beck, Sonja Jankovic, Peter C. Reinacher, Marc Hohenhaus, Horst Urbach, Martin Diebold and Theo Demerath

AJNR Am J Neuroradiol published online 26 October 2023
http://www.ajnr.org/content/early/2023/10/26/ajnr.A8022

Published October 26, 2023 as 10.3174/ajnr.A8022

Mesoscopic Assessment of Microstructure in Glioblastomas and Metastases by Merging Advanced Diffusion Imaging with Immunohistopathology

Urs Würtemberger, Daniel Erny, Alexander Rau, Jonas A. Hosp, Veysel Akgün, Marco Reisert, Valerij G. Kiselev, Jürgen Beck, Sonja Jankovic, Peter C. Reinacher, Marc Hohenhaus, Horst Urbach, Martin Diebold, and Theo Demerath

ABSTRACT

BACKGROUND AND PURPOSE: Glioblastomas and metastases are the most common malignant intra-axial brain tumors in adults and can be difficult to distinguish on conventional MR imaging due to similar imaging features. We used advanced diffusion techniques and structural histopathology to distinguish these tumor entities on the basis of microstructural axonal and fibrillar signatures in the contrast-enhancing tumor component.

MATERIALS AND METHODS: Contrast-enhancing tumor components were analyzed in 22 glioblastomas and 21 brain metastases on 3T MR imaging using DTI-fractional anisotropy, neurite orientation dispersion and density imaging–orientation dispersion, and diffusion microstructural imaging–micro-fractional anisotropy. Available histopathologic specimens (10 glioblastomas and 9 metastases) were assessed for the presence of axonal structures and scored using 4-level scales for Bielschowsky staining (0: no axonal structures, 1: minimal axonal fragments preserved, 2: decreased axonal density, 3: no axonal loss) and glial fibrillary acid protein expression (0: no glial fibrillary acid protein positivity, 1: limited expression, 2: equivalent to surrounding parenchyma, 3: increased expression).

RESULTS: When we compared glioblastomas and metastases, fractional anisotropy was significantly increased and orientation dispersion was decreased in glioblastomas (each $P < .001$), with a significant shift toward increased glial fibrillary acid protein and Bielschowsky scores. Positive associations of fractional anisotropy and negative associations of orientation dispersion with glial fibrillary acid protein and Bielschowsky scores were revealed, whereas no association between micro-fractional anisotropy with glial fibrillary acid protein and Bielschowsky scores was detected. Receiver operating characteristic curves revealed high predictive values of both fractional anisotropy (area under the curve = 0.8463) and orientation dispersion (area under the curve = 0.8398) regarding the presence of a glioblastoma.

CONCLUSIONS: Diffusion imaging fractional anisotropy and orientation dispersion metrics correlated with histopathologic markers of directionality and may serve as imaging biomarkers in contrast-enhancing tumor components.

ABBREVIATIONS: AD = axial diffusivity; AMICO = Accelerated Microstructure Imaging Via Convex Optimization; AUC = area under the curve; DMI = diffusion microstructure imaging; FA = fractional anisotropy; GBM = glioblastoma; GFAP = glial fibrillary acidic protein; ICVF = intracellular volume fraction; MD = mean diffusivity; NODDI = neurite orientation dispersion and density imaging; OD = orientation dispersion; RD = radial diffusivity; ROC = receiver operating characteristic; V-CSF = free water/CSF volume fraction; V-intra = intra-axonal volume fraction; V-ISO = isotropic volume

Glioblastomas (GBMs) and metastases are the most common malignant intra-axial brain tumors in adults. Because these entities require distinct clinical management, differentiation is important.

While the definite diagnosis is based on histopathology, MR imaging is the technique of choice for the noninvasive assessment of cerebral neoplasms. The differentiation of GBM and metastases in MR imaging is challenging though because features such as central necrosis, irregular contrast-enhanced margins, and peripheral edema may be present in both entities.[1] The distinction is particularly important when solitary intracerebral lesions are present.

Because metastases represent secondary brain tumors displacing normal brain tissue and GBMs are brain-derived tumors with

Received June 8, 2023; accepted after revision August 30.

From the Department of Neuroradiology (U.W., A.R., V.A., H.U., T.D.), Institute of Neuropathology (D.E., M.D.), Department of Diagnostic and Interventional Radiology (A.R.), Department of Neurology and Neurophysiology (J.A.H.), Department of Medical Physics (M.R., V.G.K.), Department of Stereotactic and Functional Neurosurgery (M.R., P.C.R.), and Department of Neurosurgery (J.B., M.H.), Faculty of Medicine, Medical Center–University of Freiburg, University of Freiburg, Freiburg, Germany; Department of Radiology (S.J.), Faculty of Medicine, University Clinical Center Nis, University of Nis, Nis, Serbia; Fraunhofer Institute for Laser Technology (P.C.R.), Aachen, Germany; IMM-PACT Clinician Scientist Program (M.D.), and Berta-Ottenstein-Program for Advanced Clinician Scientists (D.E.), Faculty of Medicine, University of Freiburg, Freiburg, Germany.

Martin Diebold and Theo Demerath contributed to this work equally and share last authorship.

Please address correspondence to Urs Würtemberger, MD, Department of Neuroradiology, Breisacher Straße 64, 79106 Freiburg, Germany; e-mail: urs.wuertemberger@uniklinik-freiburg.de

Indicates article with online supplemental data.

http://dx.doi.org/10.3174/ajnr.A8022

infiltrative growth, axonal components, and defined structural proteins (eg, glial fibrillary acidic protein [GFAP]), microstructural differences are conceivable within contrast-enhancing tumor areas.[2] Moreover, both tumor entities are histomorphologically well-distinguished by the presence of glial structural proteins such as GFAP, being highly abundant in GBM, but sporadic or absent in metastases,[3,4] and the extent of axonal remnants, which are frequently observed in diffusely growing gliomas but rarely in solid metastases.[5]

Current diffusion-weighted MR imaging provides the opportunity to noninvasively study the microstructure in vivo in a mesoscopic approach.[6] Our study aims to bridge the gap between the millimeter resolution of MR imaging at the voxel level and the histopathologically comprehensible structural changes at the subvoxel or micrometer level.[7] DTI is the most established technique for in vivo investigations of the brain microstructure[8] and allows graduating the directionality of diffusion, which is expressed in fractional anisotropy (FA). Numerous previous studies have shown an increase in FA within the central tumor component in GBM compared with metastases,[9-13] whereas some studies have shown inconclusive results[14,15] or even a decrease in FA in GBM.[16] FA is sensitive to anisotropic cell structures such as axons, and several studies have suggested that FA correlates with the extent of GFAP-positive astrocytes[17-19] but is also sensitive to their orientation dispersion (OD).[20] This finding is a major limitation for the use of FA as a biomarker of tissue integrity, especially in regions with complex microarchitecture. Further investigation of contrast-enhancing tumor components is also of interest because proliferative tumor components are expected there and correlation with histopathology is still lacking.

Novel, biophysically motivated advanced multicompartmental imaging techniques such as neurite orientation dispersion and density imaging (NODDI) or diffusion microstructure imaging (DMI) allow a more specific approximation of the microstructure, for example by quantifying free water[21] or the axonal density in white matter.[7] Furthermore, microFA better reflects the underlying microstructure compared with FA in areas with increased OD, independent of, for example, increased axonal fiber crossings.[20] Therefore, we aimed to additionally investigate the OD and microFA in comparison with FA.

On the basis of the distinct histologic characteristics of GBM and metastases, we hypothesized that microstructural differences between the 2 entities within the proliferative, contrast-enhancing tumor components are traceable with directionality-based diffusion metrics such as DTI-FA, NODDI-OD, and DMI-microFA and are associated with histopathology in terms of the presence of axonal and fibrillary microstructure and/or GFAP expression.

MATERIALS AND METHODS

Patient and Imaging Characteristics

This retrospective study was approved by the local institutional review board of Medical Center–University of Freiburg (EK:400/20). All procedures performed in studies involving human participants were in accordance with the ethics standards of the institutional and national research committee and with the 1964 Helsinki declaration and its later amendments. Informed written consent was waived by the local ethics committee due to the purely retrospective analysis.

Patient characteristics and ROI (contrast-enhancing tumor area) derived diffusion metrics[a]

	GBM	Metastasis	*P* Value (GBM vs Met)
No.	22	21	
Sex (male/female)	11/11	12/9	$P = .82$
Age (yr)	65.6 (12.7)	66.6 (11.8)	$P = .99$
FA	0.16 (0.04)	0.11 (0.02)	$P < .001$
OD	0.43 (0.08)	0.56 (0.10)	$P < .001$
microFA	0.29 (0.10)	0.27 (0.10)	$P = .56$

Note:—Met indicates Metastasis.
[a] Data are given as mean and standard deviation (SD).

Within 4 years (January 2018 to February 2022), a total of 43 patients with newly diagnosed brain metastases ($n = 21$) and GBMs ($n = 22$) were enrolled. Patients with relevant small-vessel disease (Fazekas > 1), concomitant vascular lesions (eg, vascular malformations), or imaging features of neurodegenerative disorders (eg, Alzheimer disease, frontotemporal lobar degeneration, cerebral amyloid angiopathy) were excluded. Similarly, previous tumor resections and brain biopsies, prior radiation therapy, and poor image quality led to study exclusion. Patient demographics and clinical details are summarized in the Table.

Imaging was conducted with 3T MR imaging scanners (Magnetom Prisma and Magnetom Prisma FIT; Siemens) using a 64-channel head and neck coil. Diffusion MR imaging sequences were acquired with the following parameters: axial orientation, 42 slices, voxel size = 1.5 × 1.5 × 3 mm^3, TR = 2800 ms, TE = 88 ms, bandwidth = 1778 Hz, flip angle = 90°, simultaneous multiband acceleration factor = 2, generalized autocalibrating partially parallel acquisition factor = 2, 65 diffusion-encoding gradient directions, 15 non-diffusion-weighted images, 2 × 58 images with b-factors = 1000 and 2000 s/mm^2. Acquisition time was 6 minutes and 22 seconds. High-resolution isotropic T1WI postcontrast sequences were acquired 4–5 minutes after IV injection of 0.1 mmol/kg of gadoteridol (Gd) (ProHance; Bracco Imaging) with 3D magnetization-prepared 180° radiofrequency pulses and a rapid gradient-echo (MPRAGE) sequence (TR = 2500 ms, TE = 2.82 ms, flip angle = 7°, TI = 1100 ms, generalized autocalibrating partially parallel acquisition factor = 2, 1.0-mm isotropic voxels, 192 contiguous sagittal slices).

A portion of the data sets (19 in the GBM, 17 in the metastases group) was used in a previous project on peritumoral diffusion measures.[22,23]

Image Postprocessing. Data processing was performed on a local instance of the postprocessing platform NORA (www.nora-imaging.org; last accessed on March 4, 2023). T1WI data sets were automatically segmented into white matter, gray matter, and CSF (with SPM12; http://www.fil.ion.ucl.ac.uk/spm/software/spm12).

Preprocessing of diffusion MR imaging data included denoising,[24] Gibbs-ringing artifacts correction,[25] and up-sampling to an isotropic resolution of 1.5 mm^3.[26] DTI measures were obtained from b=0 and 1000 s/mm^2 images using a publicly available open-source toolbox (Fibertools; https://www.uniklinik-freiburg.de/mr-en/research-groups/diffperf/fibertools.html) using the ordinary

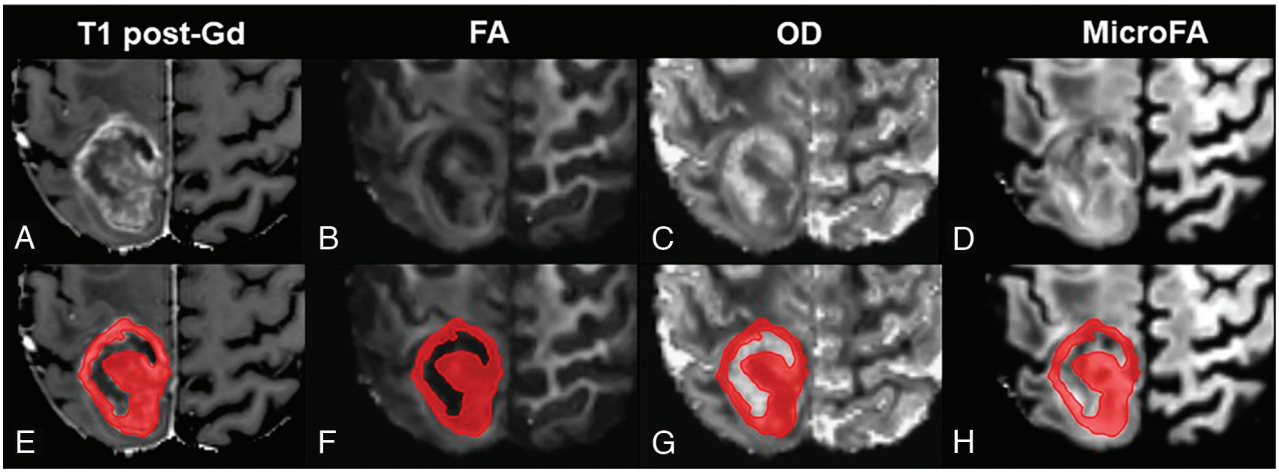

FIG 1. Presurgical (3T) MR imaging in a patient with a right parietal GBM. Representative axial images are shown in the *upper row* (*A–D*) with the corresponding ROI (of contrast-enhancing tumor components based on *A*) overlaid sections in the *lower row* (*E–H*). Gd indicates Gadoteridol.

log-linear fitting and calculating the FA and also mean, radial, and axial diffusivity. NODDI-derived OD and the intracellular and isotropic volume fractions were calculated with the Accelerated Microstructure Imaging Via Convex Optimization (AMICO) method, a regularized version of NODDI with faster processing times due to the linearization of fitting procedures.[27] DMI-based microFA and the intra-axonal (V-intra) and free water (V-CSF) volume fractions were estimated using a Bayesian approach.[20]

Image postprocessing and manual segmentation of contrast-enhancing tumor components was performed by 2 neuroradiologists (with 5 and 7 years of clinical neuroimaging experience) on 3D T1WI postcontrast data sets in coregistration with isotropic 3D T2-weighted FLAIR images to avoid erroneous segmentation of nonenhancing tumor components. First, the image data sets were checked for motion artifacts. Then, regular coregistrations of the MPRAGE and diffusion data sets were checked. Increased motion artifacts were found in 2 patients (1 per group), which led to exclusion. In addition, the coregistration was manually corrected in 1 patient (GBM group). To account for potential partial volume effects, we carefully excluded non-contrast-enhancing outer tumor margins and adjacent gray matter (Fig 1*E*).

Histopathology. Histologic analysis of contrast-enhancing tumors was performed by standardized protocols of the local institute of neuropathology. The samples analyzed in this study were obtained from radical removal surgeries of contrast-enhancing tumor portions in close temporal correlation with the analyzed MR imaging; stereotactic biopsies were not considered due to minimal/unrepresentative tissue availability. Therefore, usable histopathologic tissue samples could not be obtained for all tumors studied. A total of 19 samples (9 metastases and 10 GBMs) were processed by established diagnostic procedures for fixation in 4% paraformaldehyde, paraffin embedding, staining, and immunohistochemistry. Sections of 4-μm thickness underwent Bielschowsky silver staining to demonstrate axonal fibers, as well as immunohistochemical labeling for glial fibrillary acidic protein (GFAP) in combination with hematoxylin staining. Immunohistochemistry was performed on an Autostainer Link 48 (Agilent), according to the manufacturer's instructions with a primary antibody against GFAP (IR524; Agilent DAKO) and a corresponding secondary goat anti-rabbit immunoglobulin G4 (4050–08; SouthernBiotech).

Both readout measures were analyzed in a semiquantitative fashion by a 4-step scale regarding Bielschowsky staining (0: no axonal structures in tumor, 1: minimal axonal fragments maintained in the tumor, 2: decreased axonal density in the tumor, 3: no axonal loss in the tumor) and GFAP immunohistochemistry (0: no GFAP positivity in the tumor, 1: restricted expression in the tumor, 2: equivalent to surrounding parenchyma, 3: increased expression in the tumor). Representative images were acquired using a BX40 microscope (Olympus) and a DFC450 camera (Leica Microsystems). Figure 2 shows 1 example each of GBM and metastasis with anatomic and parametric MR imaging maps and histopathologic imaging.

Statistical Analysis. Normal data distribution was tested with the Shapiro-Wilk test. Patient age and histologic outcomes were compared between GBM and metastases using the Mann-Whitney *U* test. Sex was compared with the $\chi 2$ test between GBM and metastases groups. A one-way ANOVA was performed between contrast-enhancing areas comparing GBM and metastases groups, and a Bonferroni correction was used to account for multiple comparisons. Linear regression modeling with the Spearman rank correlation coefficient was used to relate diffusion metrics FA, OD, and microFA to semiquantitative histopathology metrics. The receiver operating characteristic (ROC) and logistic regression curves of FA, OD, and microFA of GBMs and metastases were plotted using a simple logistic regression analysis of ranked outcomes for each measure. An α-level of .05 was considered statistically significant. All statistical analyses were performed using Graphpad Prism (Version 9.3.1; GraphPad Software).

RESULTS

Study Population

A total of 43 patients (with 22 GBMs and 21 brain metastases; mean age, 65.6 and 66.6 years; 11 and 12 women, respectively) were included in this study. Of those, histopathology confirmed an *IDH* wild-type GBM in 22 patients (11 women; mean age, 65.6

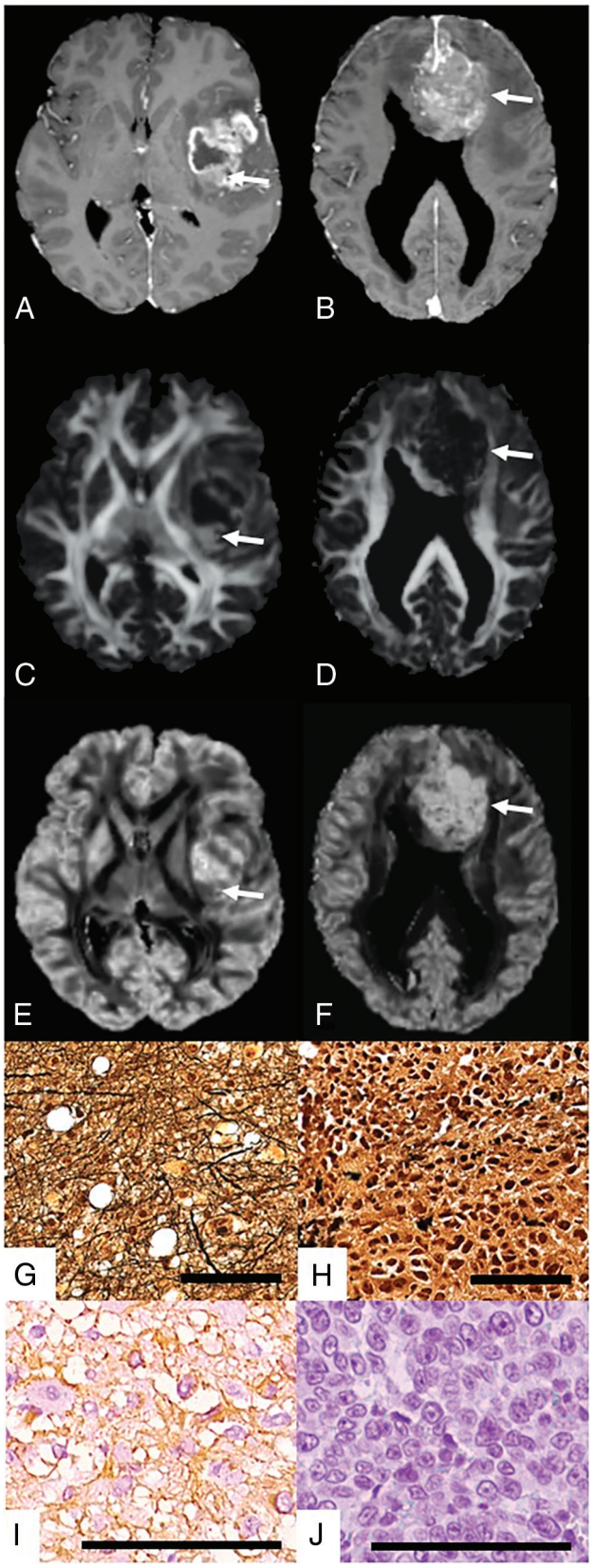

FIG 2. Representative MR images of patients with left insular GBM (*A*, T1WI post-Gd; *C*, FA; *E*, OD) and a large callosal melanoma metastasis (*B*, T1 post-Gd; *D*, FA; *F*, OD). Representative Bielschowsky silver staining to demonstrate nerve fibers and neurofibrillary tangles (*G* and *H*) and immunohistochemical labeling for GFAP (*I* and *J*). Scale bar = 100 μm.

[SD, 12.7] years; range, 41.8–88.0 years), whereas 21 patients (12 women; mean age, 66.6 [SD, 11.8] years; range, 46.5–87.2 years) had brain metastases. Primary tumors in patients with brain metastases comprised non-small-cell lung cancer ($n = 10$), small-cell lung cancer ($n = 1$), melanoma ($n = 5$), breast cancer ($n = 1$), urothelial carcinoma ($n = 1$), colorectal carcinoma ($n = 1$), esophageal carcinoma ($n = 1$), and thymus carcinoma ($n = 1$). There was no significant difference in age ($P = .96$) or sex ($P = .86$) between groups. Among these, 10 patients in the metastases cohort and 12 patients in the GBM cohort had received corticosteroids before imaging, but none of the patients had received chemotherapy or radiation therapy before imaging. Within the metastases cohort, there were 2 patients with 1 lesion, 4 patients with 2 lesions, 1 patient with 3 lesions, 1 patient with 4 lesions, 3 patients with 5 lesions, and 10 patients with 6 lesions.

Diffusion Metrics in Contrast-Enhancing Areas of Brain Metastasis and GBM

Comparison of DTI, DMI, and NODDI parameters of contrast-enhancing tumor areas revealed significantly higher FA in GBM compared with metastasis, (F [2, 89] = 548.8, $P < .001$) with a simultaneous significant decrease in OD (F [2,89] = 173.8, $P < .001$). In contrast, no significant differences in microFA between GBM and metastasis were found, whereas both microFA in GBM and metastasis was lower compared with normal-appearing white matter (F [2,89] = 92.2, $P < .001$). There was no significant difference in intracellular volume fraction (ICVF), V-intra, mean diffusivity (MD), radial diffusivity (RD), or axial diffusivity (AD) (all $P > .1$). There was in metastases, however, a significant increase in isotropic volume (V-ISO) ($P = .0025$) and a tendency toward increased V-CSF ($P = .077$). Group-related metrics and ranges are presented in the Table. The distribution of the individual values is shown in Fig 3 and the Online Supplemental Data.

Histopathology. Semiquantitative histopathologic readout scores regarding the presence of axonal structures in the tumor (Bielschowsky silver stain) and the presence of GFAP revealed distinct differences between GBM and metastases samples. In GBM samples, we visually recognized the presence of axonal structures ranging from minimal maintained axonal structures to widely intact axonal structures, whereas in tumor areas of all except 1 case with metastases, no axonal structures were found. Exemplary images are shown in the Online Supplemental Data, with detailed histology and comparison of semiquantitative assessment scores.

Correlation Analysis. Results of the Spearman correlation test revealed a positive association between the Bielschowsky score and FA ($r = 0.6761$, $P = .0053$) as well as between GFAP score and FA ($r = 0.6253$; $P = .015$). Furthermore, we identified a negative

As illustrated by parametric maps for FA (*C* and *D*, *arrows*) and OD (*E* and *F*, *arrows*), values in contrast-enhancing solid tumor components (*A* and *B*, *arrows*) approximate normal-appearing white matter in GBM. This finding is accompanied by abundant axonal structures visualized by Bielschowsky silver staining (*G*) and high GFAP expression (*I*) in GBM compared with melanoma metastasis (*H* and *J*). Scale = 100 μm.

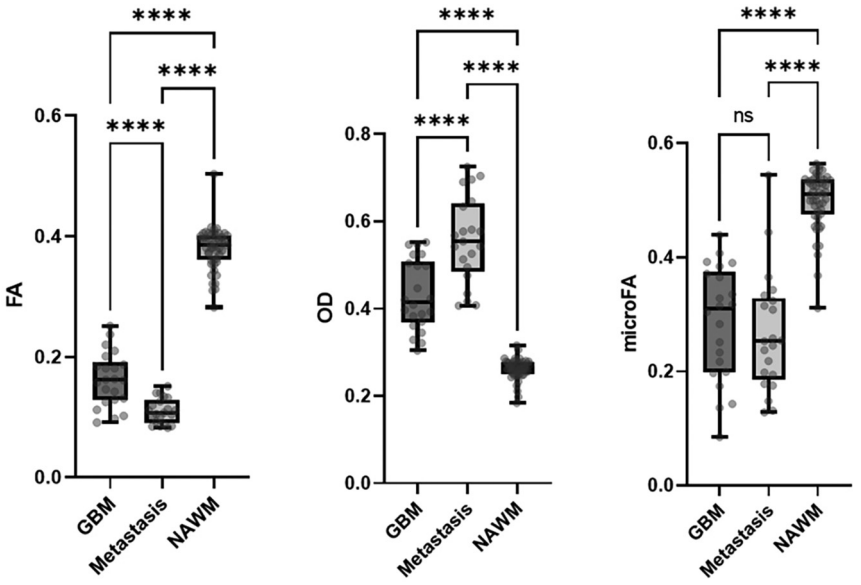

FIG 3. DTI, NODDI, and DMI metrics in contrast-enhancing tumor areas in patients with GBM ($n = 22$) and metastases ($n = 21$). Compared with metastases, GBM showed a significant shift toward increased FA and decreased OD, whereas no significant differences were found regarding microFA. *Four asterisks* indicate $P \leq .001$. NAWM indicates normal-appearing white matter.

correlation between the Bielschowsky score and OD ($r = -0.7084$, $P = .003$) and between the GFAP score and OD ($r = -0.6468$, $P = .0085$). In contrast, no significant correlations were observed between histomorphologic features and microFA (Bielschowsky score and microFA: $r = -0.08317$, $P = .7581$; GFAP score and microFA: $r = -0.1155$, $P = .6655$). Correlation plots are presented in Fig 4.

ROC and Linear Regression Analysis

Building on the systematic differences regarding FA and OD values within contrast-enhancing tumor components between GBM and metastases, we conducted an ROC analysis defining FA, OD, or microFA as dependent variables and GBM and metastases groups as class variables. This model supported the affiliation of GBM cases with higher FA values (area under the curve [AUC] = 0.8463; 95% CI, 0.73–0.96; $P < .001$). The inverse of OD appeared comparably sensitive and specific (AUC = 0.8398; 95% CI, 0.72–0.96; $P < .001$). The curve of microFA did not significantly deviate from the random classifier (AUC = 0.5736; 95% CI, 0.40–0.75; $P = .40$). ROC and logistic regression curves are presented in Fig 5.

DISCUSSION

Advanced DWI revealed distinct microstructural alterations within the contrast-enhancing tumor in GBM and metastasis regarding preserved directional diffusion in GBMs, which correlated with increased GFAP expression and axonal density in GBM. On the basis of the pattern of microstructural changes, GBM and metastases could be distinguished with sufficient accuracy.

Within the contrast-enhancing tumor area, a significant increase in FA was observed in GBM compared with metastasis. Conversely, there was a significant reduction in OD in GBM. Histopathologic assessment revealed a significant increase in GFAP expression and the presence of axonal structures in GBM, corresponding to a positive overall correlation of FA with GFAP and Bielschowsky scores and a significant negative correlation of OD with these histopathology scores in the tumor tissue. Of note, there was no significant difference in microFA between groups.

While GBMs diffusely infiltrate the brain parenchyma, spreading around a partially conserved axonal framework, metastases typically form distinct tumor masses with virtually no remnants of neuronal structures. For example, in 1 study, the peritumoral edema of GBMs was found to have a higher relative content of viable tumor cells and comparable cellularity compared with contrast-enhancing tumor,[28] whereas infiltrative growth into the tumor microenvironment up to 450 μm from the main tumor was also described in some metastases.[29] In diffuse gliomas, tumor cells have been described to extend far beyond, into macroscopically healthy brain tissue.[30,31] Previous works have suggested that quantification of free water in the peritumoral area may reflect the diffusely infiltrative nature in GBM compared with metastases,[32,33] and FA has also been used to differentiate these entities, with most studies indicating a rather low diagnostic potential of peritumoral FA[12,14,16] and only a few studies indicating increased FA within the peritumoral edema in GBM.[13] However, increased edematization of the surrounding tissue in metastases may also cause alterations in FA. Therefore, more specific parameters are required.

The contrast-enhancing solid tumor component was subject to several studies that investigated possible correlations of histopathologic parameters with MR imaging features in GBM or metastases. Increased "architectural disruption" in contrast-enhancing tumor was noted by indirectly assessing the presence of axonal structures on the basis of antibodies, though correlation of this finding with FA was lacking.[32] Even though most DTI-based studies also reported increased FA levels in contrast-enhancing tumor components in GBM compared with metastases,[9-13] there are a few studies that did not find any[14,15] or even contradictory results.[16] FA is known to be sensitive to anisotropic cell structures such as axons but also to their orientation dispersion, possibly leading to reduced FA due to increased crossing fiber tracts.[20] Therefore, the role of FA as a marker of tissue integrity may also be hampered in regions of complex microarchitecture such as in contrast-enhancing tumor.

Thus, we also examined OD and microFA. Here, we observed an inverse relationship between FA and OD, with evidence of increased OD in metastatic tissue, a plausible finding because metastases, depending on the degree of differentiation, frequently consist of unstructured cell clusters or fragmented and heterotopic tissue structures. In contrast to DTI, NODDI-based studies comparing these 2 common tumor groups are scarce to date. In

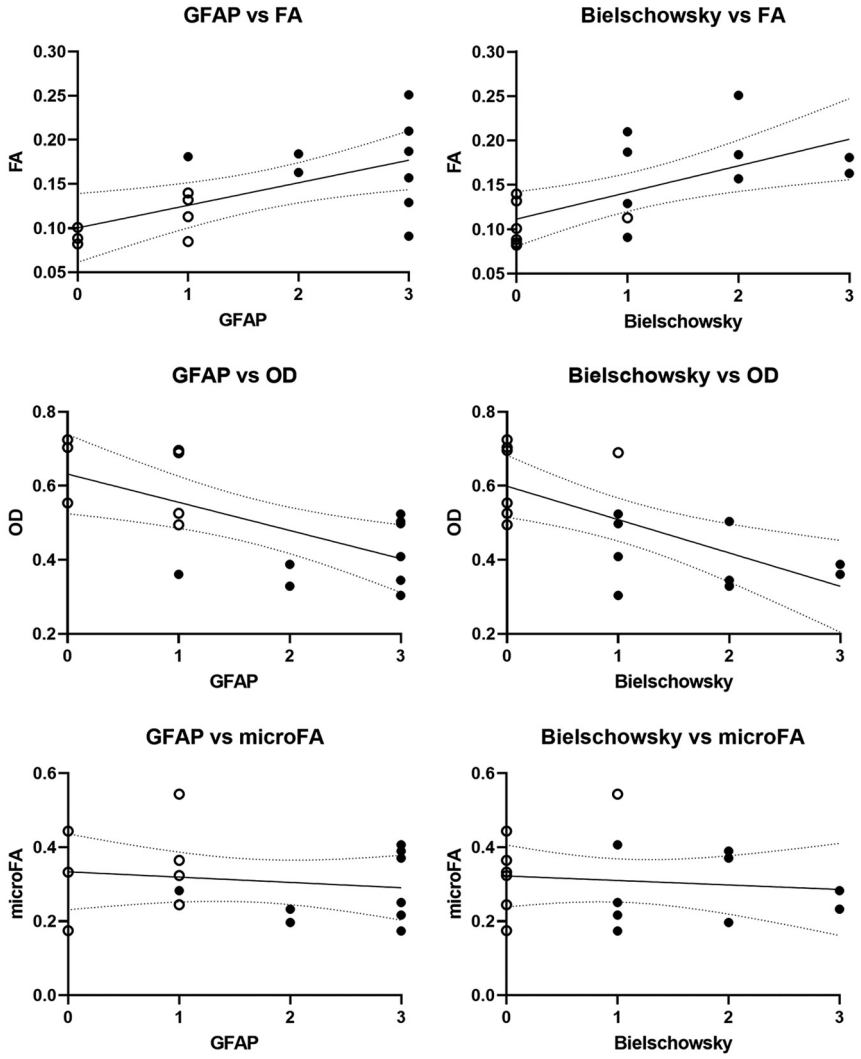

FIG 4. The Spearman rank correlation demonstrates a positive association of FA with GFAP and Bielschowsky scores (*upper row*) and a negative association of OD with GFAP and Bielschowsky scores (*middle row*). No association between microFA with GFAP and Bielschowsky scores can be detected (*lower row*). *Open circles* indicate metastasis cases; *filled circles*, GBM cases.

line with our results, lower OD was observed in high-grade gliomas,[12] whereas another NODDI-based study did not report OD.[15] Within the white matter, increased OD is thought to reflect increased axonal dispersion and degeneration, whereas a decrease in OD in gray matter may indicate dendritic thinning.[33] Therefore, the opposing signal changes of OD and FA in GBM and metastases can be well-reconciled because the presence of residual axonal structures in the contrast-enhancing tumor may tend to condition some diffusional directionality in GBM. This tendency is also supported by the significant negative correlations of OD with the increase in the Bielschowsky score, which does indeed classify the presence of axonal structures.

Because GBM and brain metastases differ with respect to the presence of axonal structures in contrast-enhancing tumor areas and OD is altered, the question arises as to why these entities do not differ in microscopic anisotropy. First, the literal interpretation of microFA represents an anticipated oversimplification. Because microFA quantifies only a single feature of microstructure (namely, the ratio of diffusivities in the principal and secondary directions), it would only coincide with FA if all microscopic tissue elements in a voxel were aligned with the parallel principal diffusion directions. Hence, FA is smaller than microFA, the higher the OD is. Moreover, as any mean value, microFA does not reflect the underlying variance. Specifically, the formal microFA values may be identical in tissue with sufficiently homogeneous microstructure and a tissue consisting of islands with high and low microFA. Such islands may further be spatially separated or related to different cellular populations, eg, axons and astrocytes. In summary, stratification of cellular morphology through microFA is limited in the diffusely growing and heterogeneous tissues assessed in this study.

In our subsequent analysis of ICVF and V-intra, we did not detect any significant difference in these estimated axonal volume fractions between the entities, even though we clearly observed histopathologic features for the presence of axons in GBM. We acknowledge that these NODDI and DMI model assumptions limit the application in intratumoral environments. The local microstructural blocks are less orientationally ordered than in normal-appearing white matter according to the significant increase in OD in tumors. Because FA summarizes the voxel-averaged microFA, the decrease in FA is fully compatible with the increase in OD; both effects are quantitatively larger in metastases. On the other hand, the work of Zhang et al[34] clearly demonstrated that there is a strong inverse relationship between FA and OD, not only in white but also gray matter, with FA also being more strongly influenced by OD than by neurite density, at least in healthy brain tissues. However, we do not disagree that optimization of advanced diffusion models to the tumor microenvironment is warranted, as already shown in the works of Panagiotaki et al[35] and Zaccagna et al,[36] applying the Vascular, Extracellular, and Restricted Diffusion for Cytometry in Tumor (VERDICT) model.

We did not find differences for MD, RD, and AD in the contrast-enhancing tumor component between GBM and metastases. The available literature is inconsistent in this regard, with 1 study also describing no differences in MD,[10] whereas another study measured lower MD and RD in high-grade gliomas.[12]

Some tentative conclusions can be drawn from our results: 1) FA of the solid tumor component may be useful as a diagnostic

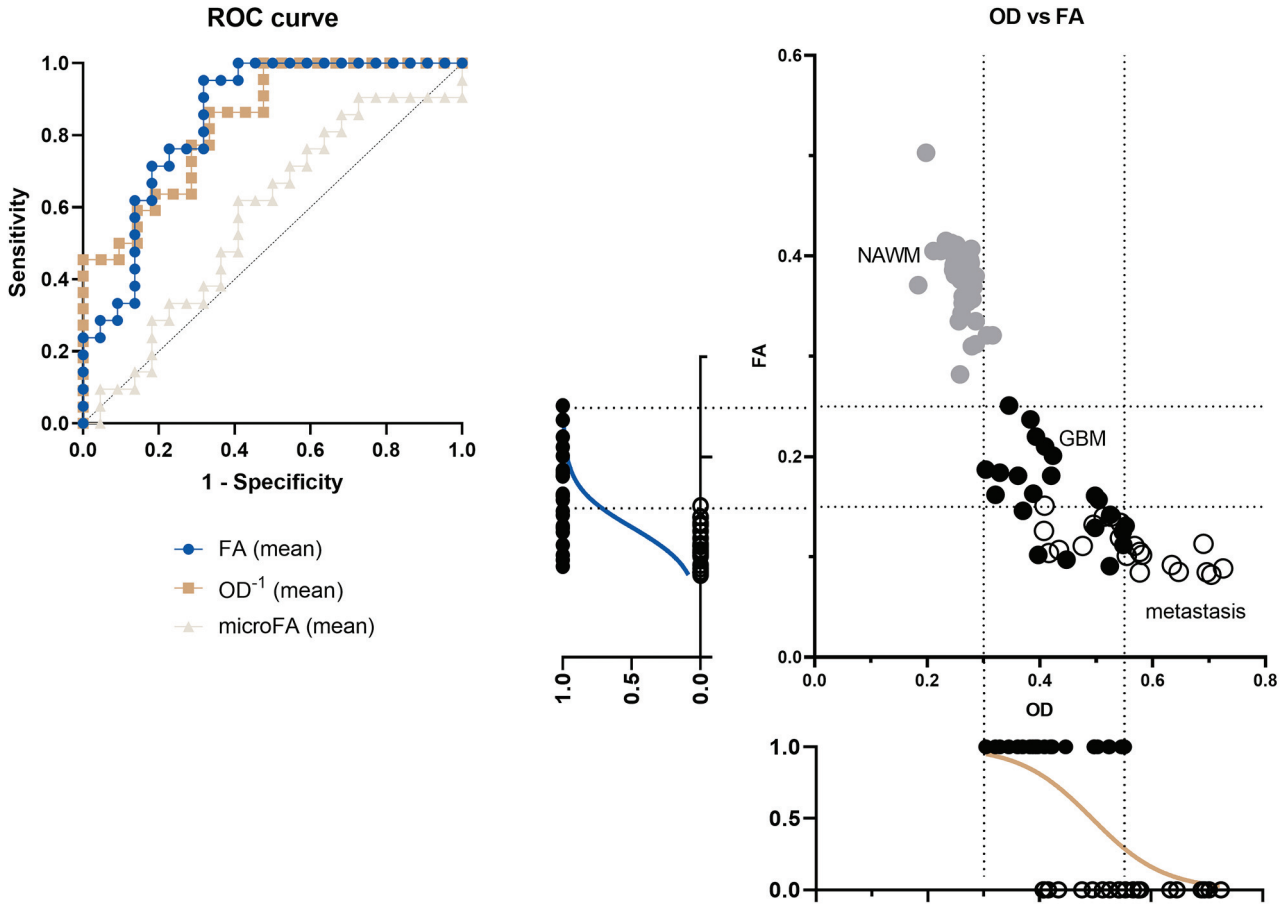

FIG 5. ROC curves of 22 patients with GBM and 21 with cerebral metastases showing a high predictive value of both FA (AUC = 0.8463) and OD (AUC = 0.8398) regarding the presence of GBM versus metastasis (*left panel*) and a scatterplot of OD and FA values for each sample (normal-appearing white matter controls = *gray filled circles*, GBM = *black filled circles*, metastasis = *open circles*) with arbitrary cutoff values of 0.3 and 0.55 for OD and 0.15 and 0.25 for FA. Logistic regression indicates the probability of GBM diagnosis compared with metastasis diagnosis at each individual OD or FA value (*right panel*).

indicator for differentiating GBM and metastases, the most common malignant neoplasms of the adult human brain. 2) In the preoperative setting, FA-based tractography is used to assess the extension of tumor components to eloquent white matter tracts such as the corticospinal or optical tract, thus anticipating risks in relation to surgically approachable lesions. The definition of these findings regarding functional relevance should be the aim of future studies.

Besides the obvious intrinsic limitations of a retrospective study, our study is further limited by the rather small patient population, and biopsies for histopathologic evaluation were available for only a subset of the cohort. Even though in the metastases cohort, almost one-half of the histopathologic primary tumors were non-small-cell lung cancer (10/21), there was still relevant heterogeneity with a total of 8 different primary tumors. Because of the additional heterogeneity between the GBM and metastasis groups due to lesion number, the aspect of differentiation based on solitary lesions was not directly addressed in the present work. However, we assume that the findings obtained can be applied to solitary (nonoverlapping) metastatic lesions.

Also, defining the contrast-enhancing tumor areas remains methodologically challenging because they can be thin, especially in GBM, and often located around a central necrotic core. To achieve the most accurate segmentation of solid tumor portions, with exclusion of necrosis, gray matter, and CSF space, we performed manual segmentation.

We assume congruence between histologic tumor specimens and MR imaging–based ROIs, which requires that tumor specimens represent contrast-enhancing components. Accidental incongruence represents a potential limitation of this study. To minimize this aspect, we used established practices with navigated techniques for resection (both in GBM and metastases) as well as necrotic areas easily identified histologically.

CONCLUSIONS

Our study reconciles the significant differences in diffusion metrics between contrast-enhanced areas in GBM and brain metastases with semiquantitatively assessed histopathologic features. Our approach demonstrates that well-established histopathologic features of axonal and glial tumor microstructure correlate with directionality-driven diffusion metrics, indicating the potential of DTI- and NODDI-based diffusion metrics for tumor discrimination.

Disclosure forms provided by the authors are available with the full text and PDF of this article at www.ajnr.org.

REFERENCES

1. Young RJ, Knopp EA. **Brain MRI: tumor evaluation.** *J Magn Reson Imaging* 2006;24:709–24 CrossRef Medline
2. Louis DN, Perry A, Wesseling P, et al. **The 2021 WHO Classification of Tumors of the Central Nervous System: a summary.** *Neuro Oncol* 2021;23:1231–51 CrossRef Medline
3. Jacque CM, Vinner C, Kujas M, et al. **Determination of glial fibrillary acidic protein (GFAP) in human brain tumors.** *J Neurol Sci* 1978;35:147–55 CrossRef Medline
4. Eng LF, Vanderhaeghen JJ, Bignami A, et al. **An acidic protein isolated from fibrous astrocytes.** *Brain Res* 1971;28:351–54 CrossRef Medline
5. Seker-Polat F, Pinarbasi Degirmenci N, Solaroglu I, et al. **Tumor cell infiltration into the brain in glioblastoma: from mechanisms to clinical perspectives.** *Cancers (Basel)* 2022;14:443 CrossRef Medline
6. Novikov DS, Jensen JH, Helpern JA, et al. **Revealing mesoscopic structural universality with diffusion.** *Proc Natl Acad Sci U S A* 2014;111:5088–93 CrossRef Medline
7. Demerath T, Donkels C, Reisert M, et al. **Gray-white matter blurring of the temporal pole associated with hippocampal sclerosis: a microstructural study involving 3 T MRI and ultrastructural histopathology.** *Cereb Cortex* 2022;32:1882–93 CrossRef Medline
8. Basser PJ, Pierpaoli C. **Microstructural and physiological features of tissues elucidated by quantitative-diffusion-tensor MRI. 1996.** *J Magn Reson* 2011;213:560–70 CrossRef Medline
9. Wang S, Kim S, Chawla S, et al. **Differentiation between glioblastomas and solitary brain metastases using diffusion tensor imaging.** *Neuroimage* 2009;44:653–60 CrossRef Medline
10. Wang S, Kim SJ, Poptani H, et al. **Diagnostic utility of diffusion tensor imaging in differentiating glioblastomas from brain metastases.** *AJNR Am J Neuroradiol* 2014;35:928–34 CrossRef Medline
11. Bette S, Huber T, Wiestler B, et al. **Analysis of fractional anisotropy facilitates differentiation of glioblastoma and brain metastases in a clinical setting.** *Eur J Radiol* 2016;85:2182–87 CrossRef Medline
12. Mao J, Zeng W, Zhang Q, et al. **Differentiation between high-grade gliomas and solitary brain metastases: a comparison of five diffusion-weighted MRI models.** *BMC Med Imaging* 2020;20:124 CrossRef Medline
13. Nguyen DH, Le TD, Nguyen HV, et al. **Discriminating glioblastoma from solitary brain metastases on 3 Tesla magnetic resonance imaging: the roles of fractional anisotropy and mean diffusivity.** *Eur Rev Med Pharmacol Sci* 2022;26:8823–31 CrossRef Medline
14. Tsougos I, Svolos P, Kousi E, et al. **Differentiation of glioblastoma multiforme from metastatic brain tumor using proton magnetic resonance spectroscopy, diffusion and perfusion metrics at 3 T.** *Cancer Imaging* 2012;12:423–36 CrossRef Medline
15. Kadota Y, Hirai T, Azuma M, et al. **Differentiation between glioblastoma and solitary brain metastasis using neurite orientation dispersion and density imaging.** *J Neuroradiol* 2020;47:197–202 CrossRef Medline
16. Wang W, Steward CE, Desmond PM. **Diffusion tensor imaging in glioblastoma multiforme and brain metastases: the role of p, q, L, and fractional anisotropy.** *AJNR Am J Neuroradiol* 2009;30:203–08 CrossRef Medline
17. Preziosa P, Kiljan S, Steenwijk MD, et al. **Axonal degeneration as substrate of fractional anisotropy abnormalities in multiple sclerosis cortex.** *Brain* 2019;142:1921–37 CrossRef Medline
18. Galbusera R, Bahn E, Weigel M, et al. **Postmortem quantitative MRI disentangles histological lesion types in multiple sclerosis.** *Brain Pathol* 2022 Dec 8. [Epub ahead of print] CrossRef Medline
19. Lee JK, Liu D, Jiang D, et al. **Fractional anisotropy from diffusion tensor imaging correlates with acute astrocyte and myelin swelling in neonatal swine models of excitotoxic and hypoxic-ischemic brain injury.** *J Comp Neurol* 2021;529:2750–70 CrossRef Medline
20. Szczepankiewicz F, Lasicō S, van Westen D, et al. **Quantification of microscopic diffusion anisotropy disentangles effects of orientation dispersion from microstructure: applications in healthy volunteers and in brain tumors**. *Neuroimage* 2015;104:241–52 CrossRef Medline
21. Rau A, Reisert M, Kellner E, et al. **Increased interstitial fluid in periventricular and deep white matter hyperintensities in patients with suspected idiopathic normal pressure hydrocephalus.** *Sci Rep* 2021;11:19552 CrossRef Medline
22. Würtemberger U, Diebold M, Erny D, et al. **Diffusion microstructure imaging to analyze perilesional T2 signal changes in brain metastases and glioblastomas**. *Cancers (Basel)* 2022;14:1155 CrossRef Medline
23. Würtemberger U, Rau A, Reisert M, et al. **Differentiation of perilesional edema in glioblastomas and brain metastases: comparison of diffusion tensor imaging, neurite orientation dispersion and density imaging and diffusion microstructure imaging**. *Cancers (Basel)* 2022;15:129 CrossRef Medline
24. Veraart J, Novikov DS, Christiaens D, et al. **Denoising of diffusion MRI using random matrix theory.** *Neuroimage* 2016;142:394–406 CrossRef Medline
25. Kellner E, Dhital B, Kiselev VG, et al. **Gibbs-ringing artifact removal based on local subvoxel-shifts.** *Magn Reson Med* 2016;76:1574–81 CrossRef Medline
26. Reisert M, Kellner E, Dhital B, et al. **Disentangling micro from mesostructure by diffusion MRI: a Bayesian approach.** *Neuroimage* 2017;147:964–75 CrossRef Medline
27. Daducci A, Canales-Rodríguez EJ, Zhang H, et al. **Accelerated Microstructure Imaging via Convex Optimization (AMICO) from diffusion MRI data**. *Neuroimage* 2015;105:32–44 CrossRef Medline
28. Eidel O, Burth S, Neumann JO, et al. **Tumor infiltration in enhancing and non-enhancing parts of glioblastoma: a correlation with histopathology.** *PLoS One* 2017;12:e0169292 CrossRef Medline
29. Berghoff AS, Rajky O, Winkler F, et al. **Invasion patterns in brain metastases of solid cancers.** *Neuro Oncol* 2013;15:1664–72 CrossRef Medline
30. Sahm F, Capper D, Jeibmann A, et al. **Addressing diffuse glioma as a systemic brain disease with single-cell analysis.** *Arch Neurol* 2012;69:523–26 CrossRef Medline
31. Venkataramani V, Schneider M, Giordano FA, et al. **Disconnecting multicellular networks in brain tumours.** *Nat Rev Cancer* 2022;22:481–91 CrossRef Medline
32. Barajas RF, Phillips JJ, Parvataneni R, et al. **Regional variation in histopathologic features of tumor specimens from treatment-naive glioblastoma correlates with anatomic and physiologic MR imaging.** *Neuro Oncol* 2012;14:942–54 CrossRef Medline
33. Zhang H, Hubbard PL, Parker GJM, et al. **Axon diameter mapping in the presence of orientation dispersion with diffusion MRI.** *Neuroimage* 2011;56:1301–15 CrossRef Medline
34. Zhang H, Schneider T, Wheeler-Kingshott CA, et al. **NODDI: practical in vivo neurite orientation dispersion and density imaging of the human brain.** *Neuroimage* 2012;61:1000–16 CrossRef Medline
35. Panagiotaki E, Walker-Samuel S, Siow B, et al. **Noninvasive quantification of solid tumor microstructure using VERDICT MRI.** *Cancer Res* 2014;74:1902–12 CrossRef Medline
36. Zaccagna F, Riemer F, Priest AN, et al. **Non-invasive assessment of glioma microstructure using VERDICT MRI: correlation with histology.** *Eur Radiol* 2019;29:5559–66 CrossRef Medline